Dear Sir or Madam,

We are pleased to inform you that the Letter

Probing the critical nucleus size in the metal-insulator phase transition of VO_2

Lei Jin *et al.*
Phys. Rev. Lett. **129**, 245701 (2022)

Published 5 December 2022

has been highlighted by the editors as an Editors' Suggestion. Publication of a Letter is already a considerable achievement, as *Physical Review Letters* accepts fewer than 1/4 of submissions, and is ranked first among physics and mathematics journals by the Google Scholar five-year h-index. A highlighted Letter has additional significance, because only about one Letter in seven is highlighted as a Suggestion due to its particular importance, innovation, and broad appeal. Suggestions are downloaded more than twice as often as the average Letter, and receive substantially more press coverage. Suggestions are cited at roughly twice the rate of nonhighlighted Letters. More information about our journal and its history can be found on our webpage prl.aps.org.

Yours sincerely,

Hugues Chaté
Editor
Physical Review Letters

Michael Thoennessen
Editor in Chief
American Physical Society

PHYSICAL REVIEW LETTERS

APS physics

Probing the Critical Nucleus Size in the Metal-Insulator Phase Transition of VO$_2$

Lei Jin,[1,2] Yin Shi,[3] Frances I. Allen,[1,4] Long-Qing Chen,[3] and Junqiao Wu[1,2,*]

[1]*Department of Materials Science and Engineering, University of California, Berkeley, California 94720, USA*
[2]*Materials Sciences Division, Lawrence Berkeley National Laboratory, Berkeley, California 94720, USA*
[3]*Department of Materials Science and Engineering, Pennsylvania State University, University Park, Pennsylvania 16802, USA*
[4]*National Center for Electron Microscopy, Molecular Foundry, Lawrence Berkeley National Laboratory, Berkeley, California 94720, USA*

In a first-order phase transition, critical nucleus size governs nucleation kinetics, but the direct experimental test of the theory and determination of the critical nucleation size have been achieved only recently in the case of ice formation in supercooled water. The widely known metal-insulator phase transition (MIT) in strongly correlated VO$_2$ is a first-order electronic phase transition coupled with a solid-solid structural transformation. It is unclear whether classical nucleation theory applies in such a complex case. In this Letter, we directly measure the critical nucleus size of the MIT by introducing size-controlled nanoscale nucleation seeds with focused ion irradiation at the surface of a deeply supercooled metal phase of VO$_2$. The results compare favorably with classical nucleation theory and are further explained by phase-field modeling. This Letter validates the application of classical nucleation theory as a parametrizable model to describe phase transitions of strongly correlated electron materials.

Nucleation is the initial step in the formation of a new thermodynamic phase in a supersaturated parent phase [1,2]. For nearly a century, it has been assumed that a successful nucleation event requires the size of the nucleus to exceed a critical nucleation size in order to stabilize the new phase, a hypothesis that constitutes the basis of classical nucleation theory (CNT) [3,4]. Nevertheless, because of the nanoscale size and transient nature of the nucleation process, as well as the difficulty to achieve supercooled matter at ultrahigh purities, direct experimental demonstration of CNT has been challenging. Very recently, Bai *et al.* [5] have shown that graphene oxide nanosheets serve as seeds to trigger ice nucleation in supercooled water droplets, but they do so only if their diameters are above certain critical sizes. The existence of these critical nucleation sizes is well expected and understood for first-order transitions in conventional condensed matter (e.g., the water-ice transition).

In contrast, the metal-insulator transition (MIT) of vanadium dioxide (VO$_2$) is fundamentally different. VO$_2$ switches from an insulating (I) phase at temperatures (T) lower than $T_{\text{MIT}} = 67\,°\text{C}$ to a metallic (M) phase at temperatures higher than T_{MIT}. The MIT is accompanied by a structural transformation from a monoclinic structure at $T < T_{\text{MIT}}$ to a tetragonal structure at $T > T_{\text{MIT}}$. The nature of the MIT in VO$_2$ is still under debate and the nucleation process of the MIT is poorly understood [6–10], with unanswered questions such as whether the MIT and the structural transformation are decoupled at the nucleation stage and follow different kinetic pathways afterward. Prior efforts have demonstrated undercooling in VO$_2$ nanoparticles consistent

with particle size as well as inferred nucleation potency distributions [11,12]. Inspired by the experimental demonstration of the applicability of CNT to water [5], in this Letter we experimentally tested CNT and probed the critical nucleation size of the I-phase nucleus in a supercooled M phase of VO$_2$. The experimental results are quantitively explained by phase-field modeling of the energetics of the process.

To probe the critical nucleation size, one must tackle the first challenge that the system needs to be in a deeply supersaturated state to have a sufficiently high thermodynamic driving force for the phase transition. We achieve this in single-crystal VO$_2$ nanobeams (thickness ∼100 nm, width ∼250 nm, length ∼50 μm) by using "irradiation shielding" via helium ion (He$^+$) irradiation. As elaborated below, here "shielding" means that VO$_2$ is locally irradiated in a way that the unirradiated part is geometrically isolated and "shielded" from external influences (e.g., contacts, substrate) that could trigger the nucleation, enabling deep supercooling for that shielded part of VO$_2$. Achieving supercooled VO$_2$ has been reported previously by applying substrate strain [13] or using graded tungsten doping [14]. However, the supercooled VO$_2$ obtained by substate strain or graded W doping exhibits a MIT deviating from the intrinsic behavior of VO$_2$. In contrast, irradiation shielding can be used to achieve deeply supercooled VO$_2$ specimens that show a "clean," intrinsic MIT, as demonstrated below. In this approach, we employ the established MIT engineering technique using He$^+$ irradiation, where the T_{MIT} of VO$_2$ is controllably reduced by He$^+$ irradiation using a

Zeiss Orion NanoFab He ion microscope (HIM) [15,16]. In the irradiation process, most of the energetic ($\sim$30 keV) He$^+$ ions penetrate through the entire thickness of the VO$_2$ nanobeams, leaving behind uniformly distributed point defects (vacancies and interstitials). The overall effect of these defects is to donate free electrons, which reduces T_{MIT} and increases the electrical conductivity (σ) of I-phase VO$_2$ [15,17–20]. This effect of reducing T_{MIT} with He$^+$ irradiation is shown in Fig. 1(a). The T_{MIT} of the nanobeam can be tuned from the natural T_{MIT} ($\sim$341 K) to near room temperature (300 K) by increasing the He$^+$ irradiation dose up to 10^{16} ions/cm^2. The irradiated VO$_2$ still maintains a high-quality MIT as manifested by the sharp jump in σ, and is fully crystalline in this dose range [15].

Taking advantage of the localized irradiation capability of the HIM, we carry out patterned irradiation along the VO$_2$ nanobeam. The schematic in Fig. 1(b) depicts the idea of irradiation shielding. A pristine, unirradiated VO$_2$ segment (gray block) is sandwiched by two He$^+$-irradiated segments (green blocks) along a single nanobeam. The platinum (Pt) bonding (gold blocks), deposited using a gallium focused ion beam (FIB) with a platinum-based organometallic precursor, secures electrical and thermal contact between the nanobeam and the underlying electrodes. The nanobeam is suspended from the substrate. In the M to I phase transition during cooling, the He$^+$-irradiated segments stay in the M phase until T is lower than their reduced T_{MIT}, following Fig. 1(a). Importantly, during this entire process, the central pristine segment also stays in the M phase, because it is shielded by the two neighboring, M-phase segments from sites that could nucleate the I phase in it, such as the substrate and the Pt contacts. It is obvious that the lowest temperature that the shielded VO$_2$ can be supercooled to (T_{sc}) is determined by the reduced
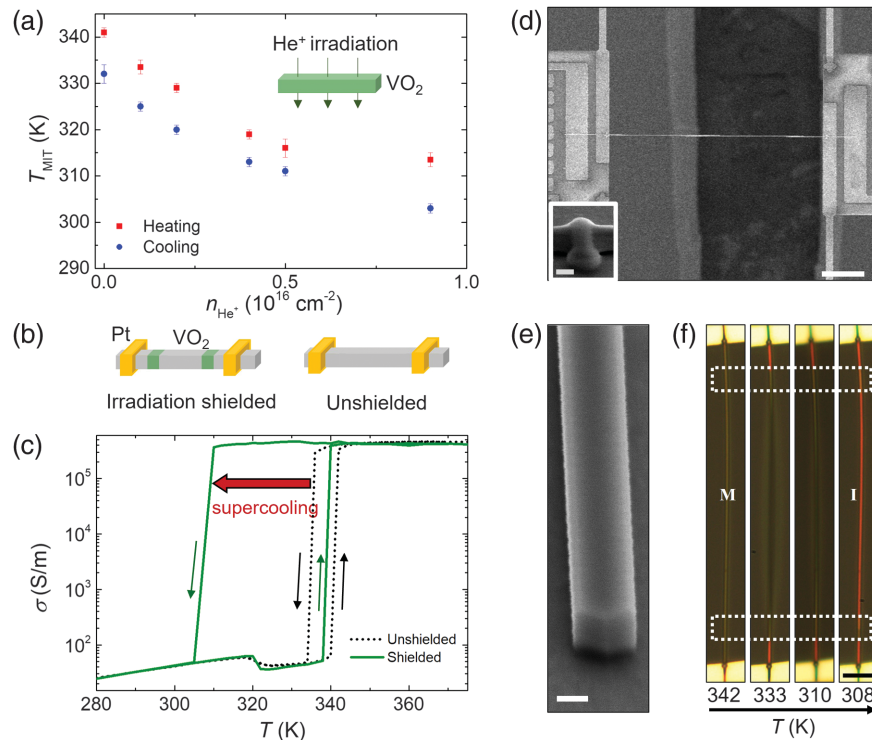
FIG. 1. Creating a deep supercooled state in the MIT of VO$_2$. (a) The MIT temperature (T_{MIT}) of VO$_2$ nanobeams as a function of the dose of He$^+$ ion irradiation. T_{MIT} is determined from electrical transport measurements. The inset shows schematically a VO$_2$ nanobeam uniformly and globally (i.e., not locally) irradiated with He$^+$ ions. (b) Schematics of He$^+$ ion irradiation for nucleation shielding in a single VO$_2$ nanobeam. The middle, pristine VO$_2$ segment (gray) is shielded against influence from the Pt contacts (yellow blocks) by two end segments of VO$_2$ that are locally He$^+$ irradiated (green). (c) Four-probe measured electrical conductivity of the same VO$_2$ nanobeams with or without irradiation shielding. Deep supercooling of the M phase down to 300 K is observed in the VO$_2$ end shielded with 5×10^{15} ions/cm^2 He$^+$ irradiation. (d) Scanning electron microscope (SEM) image of a VO$_2$ nanobeam supported by two suspended micropads. Scale bar is 10 μm. Inset: SEM image of FIB-deposited Pt bonding of the nanobeam onto the underlying electrode to minimize electrical or thermal contact resistance. Scale bar is 100 nm. (e) SEM image of a VO$_2$ nanobeam showing a rectangular cross section. Scale bar is 100 nm. (f) Optical images of a deeply supercooled, shielded VO$_2$ nanobeam as the temperature drops. A 30-μm-long VO$_2$ segment is shielded by two 4-μm-long He$^+$-irradiated segments at the two ends (indicated by the two white dashed boxes). Despite the fact that the pristine segments between the shields and the electrodes transition to I phase at normal T_{MIT} (333 K), the shielded, pristine VO$_2$ segment stays in the M phase (dark) and does not transition to the I phase (bright) until 308 K, which is close to the natural T_{MIT} (a) of the irradiated shield segments. Scale bar is 5 μm.

T_{MIT} of the shields. For comparison, a similar VO_2 nanobeam without irradiation shielding is also shown schematically in Fig. 1(b). Figure 1(c) shows the measured $\sigma(T)$ of two VO_2 nanobeams, with and without irradiation shielding, respectively. The pristine VO_2 nanobeam without irradiation shielding shows a normal MIT at ~341 K with a small hysteresis of ~8 K. The $T_{MIT} = 333$ K observed upon cooling the unshielded nanobeam is named $T_{natural}$, as it is the naturally expected T_{MIT} during cooling. In contrast, σ of the shielded VO_2 device stays metallic during cooling until 308 K, showing a deep supercooling of 25 K below the $T_{natural}$.

All VO_2 nanobeams were grown using the vapor transport method published previously [21]. They are all single crystal with rectangular cross section and smooth surface [Fig. 1(e)], maximally eliminating defects such as grain boundaries and domain walls that could nucleate the MIT. Therefore, such a shielded nanobeam, when suspended, provides an ideal supercooled platform for probing the critical nucleation size during the MIT. As shown in Fig. 1(d), two suspended micropads were used to support a nanobeam for electrical and optical measurements at variable temperatures. The micropads were suspended from the substrate with long, flexible arms, fabricated following the method published previously [22], where they were found to allow full axial strain relaxation for the supported nanobeam.

We use the visual color observed under an optical microscope to differentiate the M (dark) and I (bright) phases in the suspended VO_2 nanobeams. Figure 1(f) shows optical images of one such nanobeam during the cooling process. A 30-μm-long pristine segment is shielded by two irradiated segments (indicated by white boxes). The two irradiated segments (shields) switch to I phase once the temperature drops below 308 K, consistent with Fig. 1(a). The two segments between each of the shields and the neighboring Pt contact are pristine, and switch to I phase at 333 K, consistent with the unshielded, pristine MIT as shown in Fig. 1(c). In stark contrast, the VO_2 segment between the shields, although also pristine, remains in M phase when T decreases passing $T_{natural}$ (333 K) until T_{sc} (308 K). Within this temperature window, this shielded VO_2 segment is the ideal supercooled platform where the following experiments are carried out.

The next step is to introduce nucleation seeds with controlled sizes into the supercooled VO_2 segment. As shown in Fig. 2(a), such seeds are created by irradiating the segment with focused Ga^+ ions (FEI Quanta FIB-SEM instrument). Ga^+ irradiation is typically used to mill surfaces or cut through samples, as Ga^+ ions are heavy and when energetic can generate severe lattice damage [23], unlike the much lighter He^+ ions. In this Letter, the Ga^+ dose is limited to below 10^{17} ions/cm^2 to avoid significant surface milling (less than a few nanometers as measured by an atomic force microscope and shown in the

Supplemental Material [24]). Special care was taken to focus the Ga^+ beam only into the targeted area. The penetration depth of 30 keV Ga^+ is simulated to be 15 nm in VO_2 using the Stopping and Range of Ions in Matter (SRIM) program [25], much smaller than the thickness of the VO_2 nanobeam. The disk-shaped nucleation seeds as defined by the Ga^+ irradiated zone can be controlled by their diameter (D) and the irradiation dose (n_{Ga+}). The former is varied to probe the critical nucleation sizes, while the latter varies the surface energy to tune the capability of the seed to nucleate the I phase in supercooled, M-phase VO_2.

As shown in Fig. 2(b), a 50-μm-long single VO_2 nanobeam is patterned with eight periods of segments, where each segment consists of a 3-μm-long pristine zone as the supercooled "test bed," as well as a 3-μm-long, He^+-irradiated zone as the shield. Each shielded test bed is then implanted with one nucleation seed with specific values of D and n_{Ga+}. One test bed is free of seed ($n_{Ga+} = 0$) to allow the measurement of T_{sc}, and another small segment outside the shields is also free of seed for measuring $T_{natural}$, along the same nanobeam. During cooling, the temperature at which each supercooled test bed switches from M to I phase is named the nucleation temperature (T_{nuc}). By varying D and n_{Ga+}, we measure the corresponding T_{nuc} for each supercooled test bed. If T_{nuc} is between $T_{natural}$ and T_{sc}, the I-phase nucleation in that test bed is triggered by the nucleation seed. Figure 2(b) shows the color change of each segment when the temperature gradually decreases from $T_{natural}$ (333 K) to T_{sc} (308 K). In this experiment, n_{Ga+} is fixed at 2.2×10^{16} ions/cm^2 and D varies from 10 to 180 nm for the eight test beds. For test beds with D of 140 and 180 nm, the I phase was observed immediately at $T_{natural}$. This indicates that the nucleation seed is large enough to fully suppress the supercooling. At smaller D values, for example, 100 nm, the I phase nucleates at $T_{nuc} = 317$ K, lower than $T_{natural}$ but higher than T_{sc}. When D is smaller than ~75 nm, T_{nuc} becomes equal to T_{sc}, indicating that such nucleation seeds are too small to trigger the MIT.

For the Ga^+ doses implemented in this study, we can assume that amorphization of the irradiated disks in the VO_2 has occurred [26,27]. This is supported by our Atomic Force Microscopy (AFM) results, which show sputtering of a few nanometer in depth, indicating that the dose threshold for amorphization has been well surpassed. We note that the actual ion dose profiles and hence the effective seed diameters depend on the Gaussian beam profile of the incident beam, the lateral straggle of the ions interacting with the VO_2, and the scan setting used to pattern each disk. These effects are described in detail in the Supplemental Material [24]. We find that for nominal disk diameters of 25 nm and above, the full width at half maximum of the effective dose profiles are in close agreement with the nominal diameters (within one nanometer).
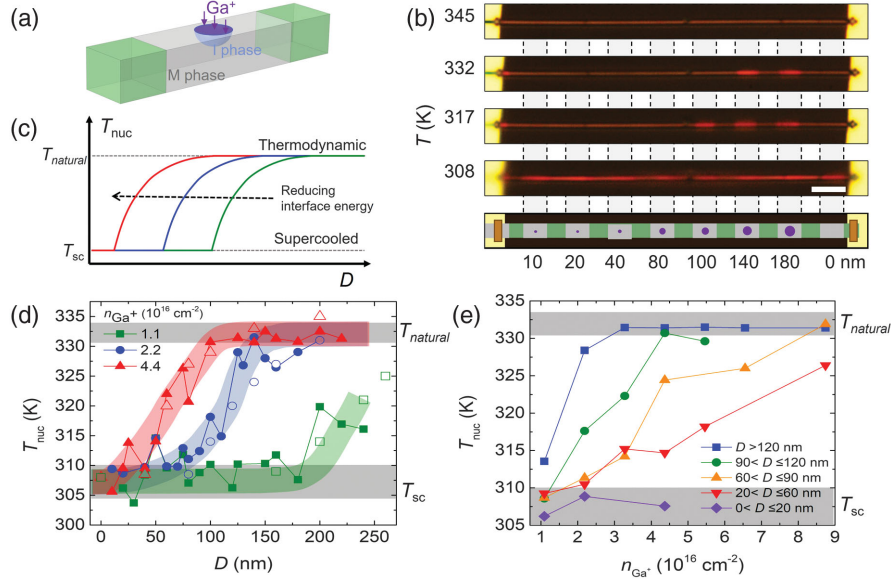
FIG. 2. *I*-phase nucleation in supercooled VO$_2$. (a) Schematic showing a disk-shaped nucleation seed (purple) created by Ga$^+$ ion irradiation on the surface of a shielded pristine VO$_2$ segment. The Ga$^+$ ion penetration depth is $\sim$15 nm, very shallow compared to the diameter of the irradiated area; hence the nucleation can be approximated as a disk shape with zero thickness. (b) Optical image of the *I*-phase nucleation process along a long, suspended VO$_2$ nanobeam. The nanobeam is divided into eight pristine segments, each shielded by two He$^+$-irradiated segments, then a nucleation seed is introduced onto the surface of each of the pristine segments by Ga$^+$ irradiation at a dose of 2.2×10^{16} ions/cm^2, but with different diameters. The lowest panel shows schematically the case where the diameter of the disk-shaped nucleation seed (D) increases from 10 to 180 nm. Scale bar is 5 μm. (c) Schematic dependence of *I*-phase nucleation temperature (T_{nuc}) on D, as predicted by classical nucleation theory. T_{nuc} is upper bounded by the natural MIT temperature (T_{natural}) and lower bounded by the supercooled temperature (T_{sc}) of the shielded VO$_2$. With reduced interface energy, stable nuclei with smaller D are able to form at a given temperature. (d) Measured (solid symbols) and calculated (open symbols) T_{nuc} as a function of D for different Ga$^+$ irradiation doses. The thick curved bands are a guide for the eye. The critical sizes of the nucleus can be determined from the onset of the rise above the supercooled limit. (e) Measured dependence of T_{nuc} on Ga$^+$ irradiation dose ($n_{\text{Ga+}}$) in the seed at different D intervals. A heavier dose in the seed promotes *I*-phase nucleation as shown by the increased T_{nuc}. T_{nuc} for nucleation seeds with large D and high doses is found to reach the thermodynamic limit. T_{natural} and T_{sc} are marked by the gray shaded areas in (d) and (e).

We use classical nucleation theory to analyze the critical nucleation diameter ($2r_c$) as a function of T_{nuc}. According to CNT, the change in the Gibbs free energy ΔG for forming a new *I* phase in a supercooled *M* phase is expressed as [4]

$$\Delta G = \frac{2}{3}\pi r^3 \cdot \Delta g_v + 2\pi r^2 \cdot \beta + \pi r^2 \cdot \gamma, \quad (1)$$

where r is the radius of the *I*-phase nucleus, Δg_v is the difference in volumetric Gibbs free energy, β is the interface energy between the *I* and *M* phases, and γ is the interface energy between the *I* phase and the nucleation seed. For simplicity, the *I*-phase nucleus is assumed to be hemispherical, growing from the disk-shaped nucleation seed as shown in Fig. 2(a). From $d\Delta G/dr = 0$, the critical radius is found to be

$$r_c = \frac{2(\beta + \gamma/2)}{|\Delta g_v|}. \quad (2)$$

In addition [4],

$$\Delta g_v = \frac{\Delta h_f(T_{\text{natural}} - T_{\text{nuc}})}{T_{\text{natural}}}, \quad (3)$$

where Δh_f is the volumetric enthalpy of nucleus formation. Subsequently,

$$r_c = \left| \frac{2(\beta + \gamma/2)}{\Delta h_f} \right| \left(\frac{1}{1 - T_{\text{nuc}}/T_{\text{natural}}} \right) \quad (4)$$

and

$$T_{\text{nuc}} = T_{\text{natural}} \cdot \left[1 - \left| \frac{2(\beta + \gamma/2)}{\Delta h_f} \right| \left(\frac{1}{r_c} \right) \right]. \quad (5)$$

The dependence of T_{nuc} on r_c is shown schematically in Fig. 2(c). T_{nuc} is bounded by the thermodynamic limit T_{natural} and the supercooling limit T_{sc}. At these two limits, T_{nuc} no longer depends on D. Between these two limits, the *I*-phase nucleation is triggered by the seed at T_{nuc} when D is comparable to the critical nucleation size $2r_c$. The *I* phase is more likely to nucleate at seeds with larger D and higher $n_{\text{Ga+}}$. Higher lattice disorder in the nucleation seed arising from higher $n_{\text{Ga+}}$ reduces the energy barrier to trigger the

nucleation. This is depicted as a shift of the $T_{nuc}(D)$ curve toward smaller D with reduced γ, as shown in Fig. 2(c).

T_{nuc} is experimentally measured by independently varying both n_{Ga+} (from 1.1 to 8.8×10^{16} ions/cm^2) and D (from 5 to 260 nm). Figure 2(d) plots T_{nuc} as a function of n_{Ga+} for fixed ranges of D. A monotonic increase in T_{nuc} is observed with n_{Ga+}, suggesting promoted nucleation with higher n_{Ga+}. T_{nuc} is saturated at $T_{natural}$ for D larger than 120 nm and n_{Ga+} higher than 3.3×10^{16} ions/cm^2. This is the condition of full suppression of the supercooling. If D is smaller than 20 nm or n_{Ga+} is lower than 1.1×10^{16} ions/cm^2, T_{nuc} saturates at T_{sc}, and no I-phase nucleus can be stabilized at the implanted seeds. Figure 2(e) plots T_{nuc} as a function of D for fixed n_{Ga+}, which shows good agreement with the dependence expected from CNT [Fig. 2(c)]. The shift of curves with higher n_{Ga+} to smaller D indicates that the increase in n_{Ga+} reduces the effective interface energy, presumably via a reduction in γ.

To quantitatively analyze the data, we use a previously developed phase-field model of VO$_2$ [28–31] to calculate the nucleation temperatures of the I phase in freestanding VO$_2$ nanobeams. This model describes the mesoscopic properties of VO$_2$ in terms of a structural order parameter field η (characterizing the lattice structural phases), an electronic order parameter field ψ (characterizing the insulating or metallic phases), the free carrier densities, and the elastic strain field. We simplify the model by setting the free carrier densities to be at equilibrium and the elastic energy to zero, because we are only concerned with equilibrium states and the strain in the freestanding nanobeams is fully relaxed. We then set up a VO$_2$ cube with a side length of 300 nm with a stress-free boundary condition imitating part of a freestanding VO$_2$ nanobeam. The initial state is set to that of a hemispherical I-phase nucleus with a given diameter embedded into the surface of the M-phase cube. We then tune the temperature and observe whether the nucleus grows or shrinks to find the nucleation temperature. We take into account the interface energy between the I phase and the Ga$^+$-irradiated VO$_2$, γ, by renormalizing the gradient energy coefficient (characterizing the domain wall energy) in the phase-field model. γ is related to the renormalized domain wall energy β_t and the true I-M domain wall energy β via $\gamma = 2(\beta_t - \beta)$, which simply results from the approximation that the shape of the I-phase nucleus is close to a hemisphere. We fit the calculated nucleation temperature as a function of the nucleus diameter to the experimentally measured relation by adjusting the renormalized gradient energy coefficient. The calculated results are shown as open symbols in Fig. 2(d). The yielded γ's are 1.39, 0.606, and 0.282 J/m^2 for the Ga$^+$ irradiation doses of 1.1, 2.2, and 4.4×10^{16} ions/cm^2, respectively. The good quantitative agreement between the measured and calculated results strongly supports that the CNT well describes the MIT in VO$_2$.
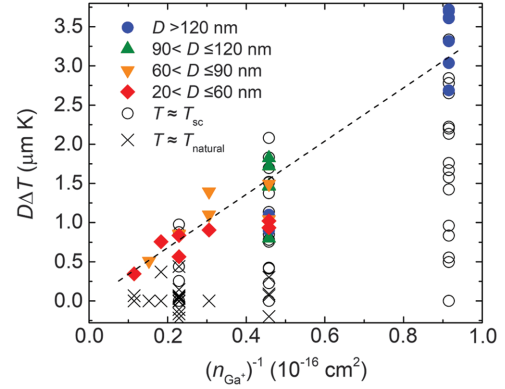
FIG. 3. Measured $D\Delta T$ of all nucleation seeds with different diameters as a function of the reciprocal Ga$^+$ dose density. The black cross hairs and black open circles are $D\Delta T$ data measured from the nucleation seeds that drive the VO$_2$ to the thermodynamic or natural and supercooled limit, respectively. Between these two limits (solid and colored symbols), T_{nuc} depends on D and the dose of the nucleation seeds. A linear fit of all colored symbols (black solid line) indicates that the interface energy ($\propto D\Delta T$) of the nucleation seeds is inversely proportional to their Ga$^+$ irradiation dose density n_{Ga+}.

Furthermore, based on Eqs. (4) or (5), the total interface energy can be expressed as

$$\beta + \gamma/2 = \frac{|\Delta h_f|}{2T_{natural}} r_c (T_{natural} - T_{nuc}). \qquad (6)$$

Between the thermodynamic (natural) and supercooling limits, $D \approx 2r_c$. Given that Δh_f and $T_{natural}$ are constant, it is clear that $D\Delta T \propto \beta + \gamma/2$, where $\Delta T = T_{natural} - T_{nuc}$. In Fig. 3, the measured $D\Delta T$ is plotted as a function of $1/n_{Ga+}$, where colored symbols represent data with I-phase nucleation occurring between (i.e., not reaching) the thermodynamic and supercooling limits. These colored data points can be fitted with a linear dependence on $1/n_{Ga+}$. Such a dependence shows an empirical relationship between the Ga$^+$ irradiation dose (n_{Ga+}) and the lowering of the interface energy γ. As the interface is one between crystalline VO$_2$ and the irradiation amorphized VO$_2$, future work to elucidate the mechanism behind this relationship might provide a useful knob to control the MIT at the level of a single nucleation event.

In conclusion, we show that classical nucleation theory governs the kinetic nucleation process in the coupled structural-electronic phase transition in a strongly correlated electron material. The critical nucleation size in the transition is determined experimentally, and found to be as small as tens of nanometers depending on the interface energy of the heterogeneous nucleus. A deeply supercooled VO$_2$ test bed is created by shielding it from other nucleation sites using He$^+$ ion irradiation. A nucleation seed is introduced to the test bed by surface irradiation with energetic Ga$^+$ ions. The achieved deep supercooling state

in the pristine, single-crystal and strain-free VO_2 may also serve as a clean platform for probing the intrinsic properties of its metal-insulator transition.

---

[*]wuj@berkeley.edu

[1] D. Kashchiev, *Nucleation* (Elsevier, New York, 2000).

[2] P. G. Vekilov, Cryst. Growth Des. **10**, 5007 (2010).

[3] H. Vehkamäki, *Classical Nucleation Theory in Multicomponent Systems* (Springer Science & Business Media, Berlin, 2006).

[4] V. I. Kalikmanov, *Nucleation Theory* (Springer, New York, 2013), pp. 17–41.

[5] G. Bai, D. Gao, Z. Liu, X. Zhou, and J. Wang, Probing the critical nucleus size for ice formation with graphene oxide nanosheets, Nature (London) **576**, 437 (2019).

[6] R. M. Wentzcovitch, W. W. Schulz, and P. B. Allen, VO_2: Peierls or Mott-Hubbard? A View from Band Theory, Phys. Rev. Lett. **72**, 3389 (1994).

[7] J. B. Goodenough, The two components of the crystallographic transition in VO_2, J. Solid State Chem. **3**, 490 (1971).

[8] S. Kim, K. Kim, C.-J. Kang, and B. Min, Correlation-assisted phonon softening and the orbital-selective Peierls transition in VO_2, Phys. Rev. B **87**, 195106 (2013).

[9] J. D. Budai *et al.*, Metallization of vanadium dioxide driven by large phonon entropy, Nature (London) **515**, 535 (2014).

[10] T. Yao *et al.*, Understanding the Nature of the Kinetic Process in a VO_2 Metal-Insulator Transition, Phys. Rev. Lett. **105**, 226405 (2010).

[11] R. Lopez, T. Haynes, L. Boatner, L. Feldman, and R. Haglund, Jr., Size effects in the structural phase transition of VO_2 nanoparticles, Phys. Rev. B **65**, 224113 (2002).

[12] H. Clarke, B. D. Caraway, D. G. Sellers, E. J. Braham, S. Banerjee, R. Arróyave, and P. J. Shamberger, Nucleation-controlled hysteresis in unstrained hydrothermal VO_2 particles, Phys. Rev. Mater. **2**, 103402 (2018).

[13] W. Fan, J. Cao, J. Seidel, Y. Gu, J. W. Yim, C. Barrett, K. M. Yu, J. Ji, R. Ramesh, L. Q. Chen, and J. Wu, Large kinetic asymmetry in the metal-insulator transition nucleated at localized and extended defects, Phys. Rev. B **83**, 235102 (2011).

[14] Sangwook Lee, Chun Cheng, Hua Guo, Kedar Hippalgaonkar, Kevin Wang, Joonki Suh, Kai Liu, and Junqiao Wu, Axially engineered metal–insulator phase transition by graded doping VO_2 nanowires, J. Am. Chem. Soc. **135**, 4850 (2013).

[15] L. Jin, S. E. Zeltmann, H. S. Choe, H. Liu, F. I. Allen, A. M. Minor, and J. Wu, Disorder recovers the Wiedemann-Franz law in the metallic phase of VO_2, Phys. Rev. B **102**, 041120(R) (2020).

[16] F. I. Allen, A review of defect engineering, ion implantation, and nanofabrication using the helium ion microscope, Beilstein J. Nanotechnol. **12**, 633 (2021).

[17] J. Jeong, N. Aetukuri, T. Graf, T. D. Schladt, M. G. Samant, and S. S. P. Parkin, Suppression of metal-insulator transition in VO_2 by electric field-induced oxygen vacancy formation, Science **339**, 1402 (2013).

[18] J. G. Ramirez, T. Saerbeck, S. Wang, J. Trastoy, M. Malnou, J. Lesueur, J.-P. Crocombette, J. E. Villegas, and I. K. Schuller, Effect of disorder on the metal-insulator transition of vanadium oxides: Local versus global effects, Phys. Rev. B **91**, 205123 (2015).

[19] D. Lee *et al.*, Isostructural metal-insulator transition in VO_2, Science **362**, 1037 (2018).

[20] Zhenhua Zhang, Hua Guo, Wenqiang Ding, Bin Zhang, Yue Lu, Xiaoxing Ke, Weiwei Liu, Furong Chen, and Manling Sui, Nanoscale engineering in VO_2 nanowires via direct electron writing process, Nano Lett. **17**, 851 (2017).

[21] C. Cheng, K. Liu, B. Xiang, J. Suh, and J. Wu, Ultra-long, free-standing, single-crystalline vanadium dioxide micro/nanowires grown by simple thermal evaporation, Appl. Phys. Lett. **100**, 103111 (2012).

[22] S. Lee *et al.*, Anomalously low electronic thermal conductivity in metallic vanadium dioxide, Science **355**, 371 (2017).

[23] D. Drobne, M. Milani, V. Lešer, and F. Tatti, Surface damage induced by FIB milling and imaging of biological samples is controllable, Microsc. Res. Tech. **70**, 895 (2007).

[24] See Supplemental Material at http://link.aps.org/supplemental/10.1103/PhysRevLett.129.245701 for surface morphology and irradiation analysis, as well as data and images at additional temperatures.

[25] J. F. Ziegler, M. D. Ziegler, and J. P. Biersack, SRIM—The stopping and range of ions in matter (2010), Nucl. Instrum. Methods Phys. Res., Sect. B **268**, 1818 (2010).

[26] H. Mei *et al.*, Tuning carrier density and phase transitions in oxide semiconductors using focused ion beams, Nanophotonics **11**, 3923 (2022).

[27] J. Rensberg *et al.*, Active optical metasurfaces based on defect-engineered phase-transition materials, Nano Lett. **16**, 1050 (2016).

[28] Y. Shi, F. Xue, and L.-Q. Chen, Ginzburg-Landau theory of metal-insulator transition in VO_2: The electronic degrees of freedom, Europhys. Lett. **120**, 46003 (2017).

[29] Y. Shi and L.-Q. Chen, Current-Driven Insulator-to-Metal Transition in Strongly Correlated VO_2, Phys. Rev. Appl. **11**, 014059 (2019).

[30] Yin Shi, Amy E. Duwel, Dennis M. Callahan, Yifei Sun, F. Anika Hong, Hari Padmanabhan, Venkatraman Gopalan, Roman Engel-Herbert, Shriram Ramanathan, and Long-Qing Chen, Dynamics of voltage-driven oscillating insulator-metal transitions, Phys. Rev. B **104**, 064308 (2021).

[31] Y. Shi and L.-Q. Chen, Intrinsic Insulator-Metal Phase Oscillations, Phys. Rev. Appl. **17**, 014042 (2022).

Supplementary Information

Probing the critical nucleus size in the metal-insulator phase transition of VO$_2$

1. AFM of Ga-irradiated regions
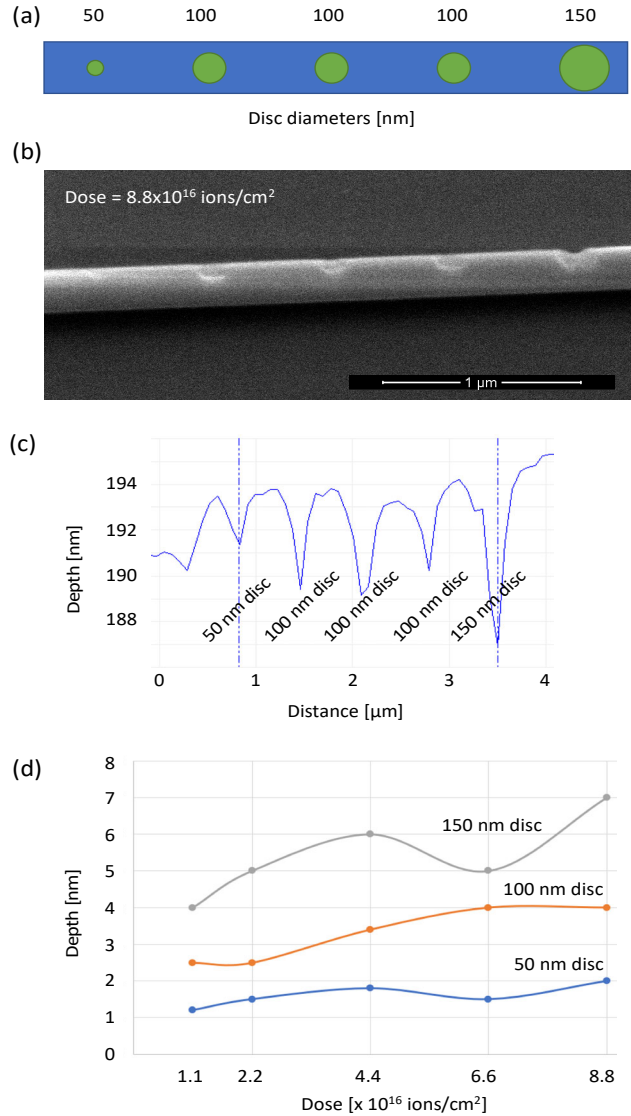
Figure S1: AFM study of Ga-irradiated discs. (a) Schematic showing disc sizes tested. (b) SEM image of Ga-irradiated discs in VO$_2$ beam using dose of 8.8x10^{16} ions/cm^2. (c) Corresponding AFM line profile through the center of the discs. (d) AFM depths obtained for a range of disc sizes and ion doses. Lines are used to connect the data points.

AFM depth profiling of discs irradiated to different doses was performed and the results are summarized in Fig. S1. Within the ion dose range implemented in this study it becomes clear that in all cases milling of the VO$_2$ on the order of a few nanometers has occurred. Since the ion dose threshold for sputtering is higher than that of subsurface amorphization *(1)*, we conclude that

amorphization has occurred in all discs. Furthermore, reference to the literature indicates that our ion doses (in the 10^{16} ions/cm^2 range) were actually two orders of magnitude higher than the threshold dose for amorphization of VO$_2$ with 30 kV Ga$^+$ *(2,3)*.

In Fig. S1(d), it is interesting to note that milling depth also depends on the width of the patterned disc. i.e. not only on the ion dose. This is likely due to redeposition of sputtered material from the sidewalls of the discs, which is more significant for the smaller disc sizes.

2. Consideration of effective diameters of the Ga-irradiated discs

The nucleation seed diameters stated in the manuscript are nominal values, obtained from the FIB patterning software. However, the beam profile in the sample needs to be considered, since this will determine the actual radial dose profiles. In order to do this, we need to take two contributions into account: 1) the beam profile of the incident gallium ion beam, and 2) the lateral straggle of the ions upon interaction with the sample. Each profile can be approximated by a Gaussian:

- The FWHM of the incident beam can be taken to be 7 nm (value provided by the FIB manufacturer for the 30 kV, 1.5 pA beam used in this study).

- The FWHM of the lateral straggle of the ions in the sample can be estimated from Monte Carlo simulations using Stopping of Ions in Matter (SRIM) code *(4)*. As shown in the SRIM results below, this FWHM can be assumed to be 6 nm (30 kV Ga ions incident on monoclinic VO$_2$ of density 4.57 g/cm^3).
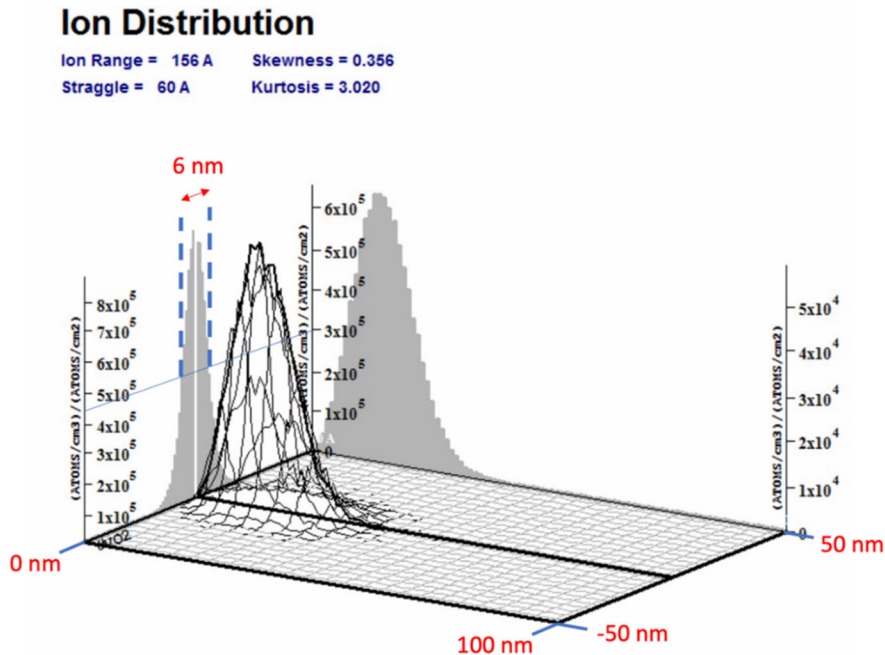
Figure S2: Ion distribution from SRIM simulation of 30 kV Ga ions incident on monoclinic VO$_2$.

In order to compute the effective ion dose profiles for the patterned discs, we combine the Gaussians from 1) and 2). The variance of the new Gaussian equals the sum of the variances of the constituent Gaussians and for the new Gaussian we obtain a FWHM 7.81 nm.

We can compute 1D dose profiles taking into account the scan spacings used by the patterning software. The default beam overlap is 50%, giving a scan spacing of 3.5 nm. For a line scan consisting of six scan points (red curves in Fig. S3 below), the resulting 1D dose profile (blue curve) is as follows:
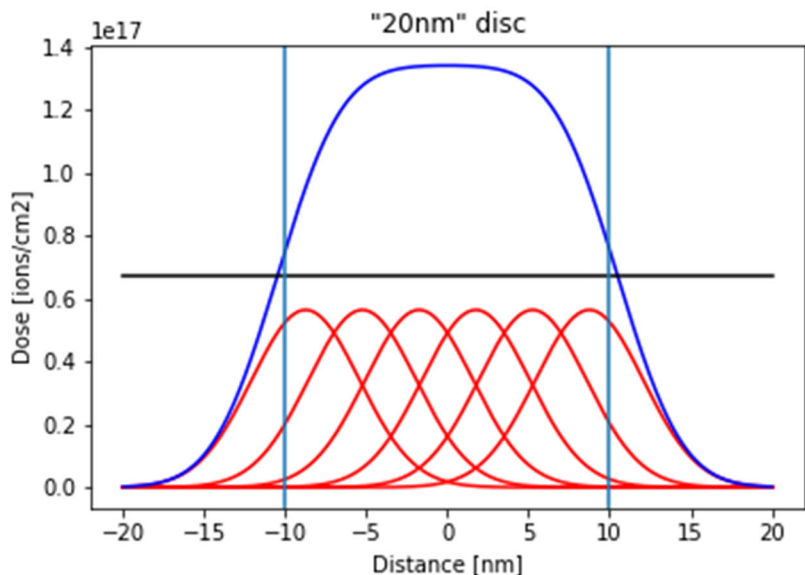
Figure S3: 1D dose profile for line scan comprising 6 scan points with a scan spacing of 3.5 nm.

The horizontal black line in the plot marks the half-maximum threshold of the dose profile - the FWHM of the blue curve is 21 nm. To a first approximation, this 1D scan can be thought of as the diameter of a nominal (as programed) 20 nm disc.

In order to estimate the effective dose profiles of the actual discs, the 2D scenario (i.e. a mesh of scan points) must be considered, as shown in Fig. S4. 2D Gaussian profiles (FWHM 7.81 nm, from above) have been inserted at each dwell point and the contour plots show the resulting dose distributions for a range of disc sizes. In the case of a disc with programed diameter 5 nm (red circle), we infer a single dwell point. This results in an ion distribution with FWHM 7.81 nm (black circle). Thus clearly in the case of this small disc, there is a significant offset between the nominal and the effective disc diameter. For the nominal 10 nm disc, the effective diameter (FWHM) is 9.08 nm, and for the nominal 20 nm disc, the effective diameter (FWHM) is 18.28 nm. As we move to even larger discs (nominal diameters of 25 nm and above), the offset is consistently < 1nm.

Thus, concerning the disc diameters stated in the manuscript, we find that the FWHM of the effective dose profiles are in close agreement for nominal disc diameters of 25 nm and above, but that for smaller discs, it should be borne in mind that there will be an offset between the

nominal and effective disc diameters due to the error introduced by the smaller number of scan points.
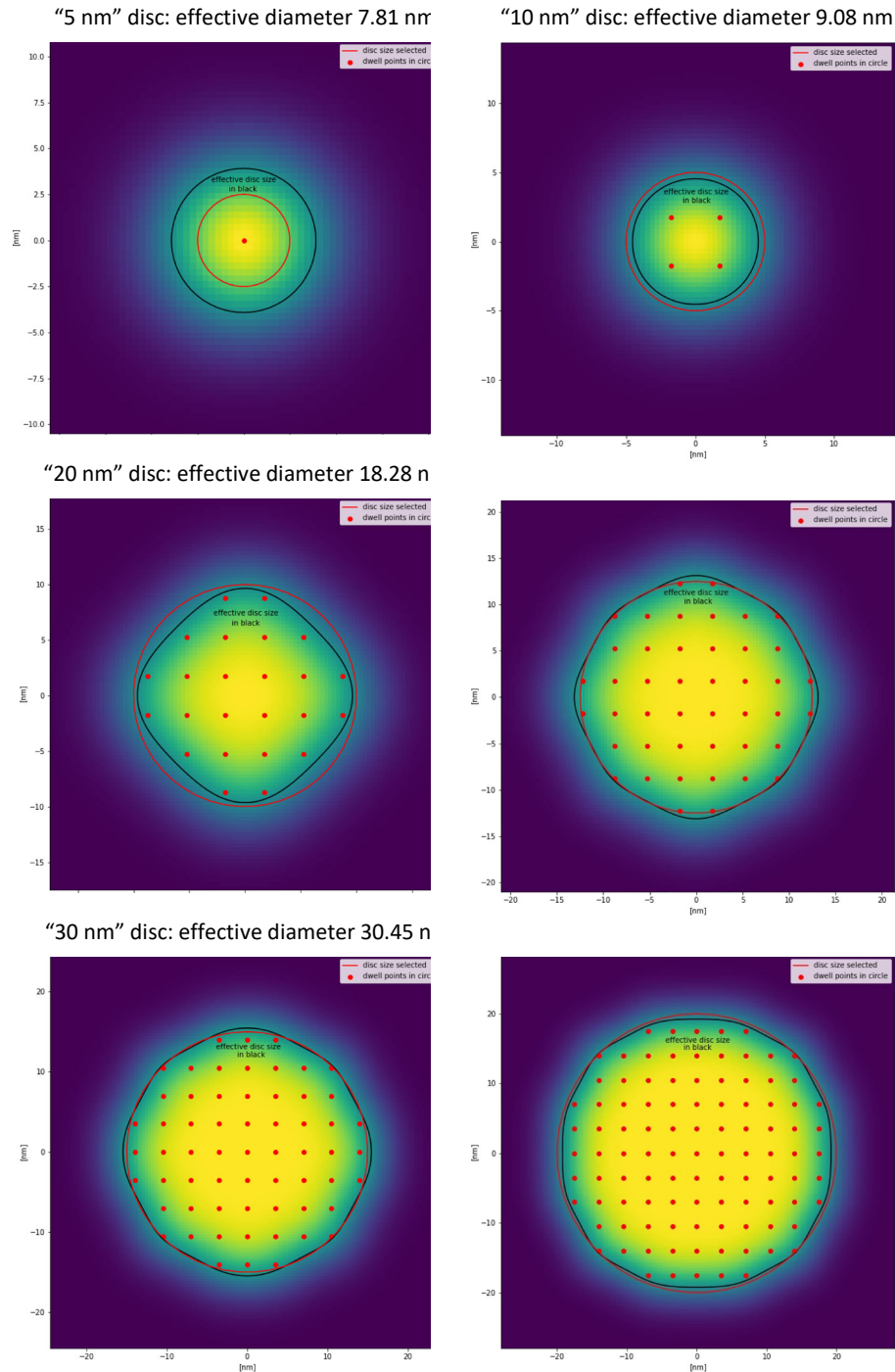
Figure S4: Contour plots showing computed 2D dose profiles for various disc diameters. Red dots indicate scan points (scan spacing 3.5 nm), red circles indicate the nominal (as programed) disc diameters, and black lines indicate the FWHM contours of the effective 2D dose profiles (the average FWHM values are given above each subfigure).

4

Inspecting the contour plots in Fig. S4 further, we see that relative to the disc diameters, the decay in dose around the edges is fairly steep. This can be seen more clearly in the line profile plots shown in Fig. S5a (computed from the ion distribution contour plots for the 10, 20, 40 and 100 nm discs). In Fig. S5b we consider how the line profiles change with increasing dose for a fixed disc size of 40 nm. The FWHM is of course independent of dose, but if we assume a certain threshold value for the material transformation (horizontal black line in the figure), we see that the crossing points with the three dose profiles are shifted by a few nanometers. Therefore, if the actual disc diameters are determined by this threshold, then the effective diameter increases with dose. Of course the position of this threshold line will determine the magnitude of the shift, but given the rate of decay in ion dose at the edges of the discs, we believe that for the purposes of the current study it is reasonable to assume that regardless of dose, the size of the nucleation seed can be approximated by the nominal disc diameter (for nominal diameters >25 nm).
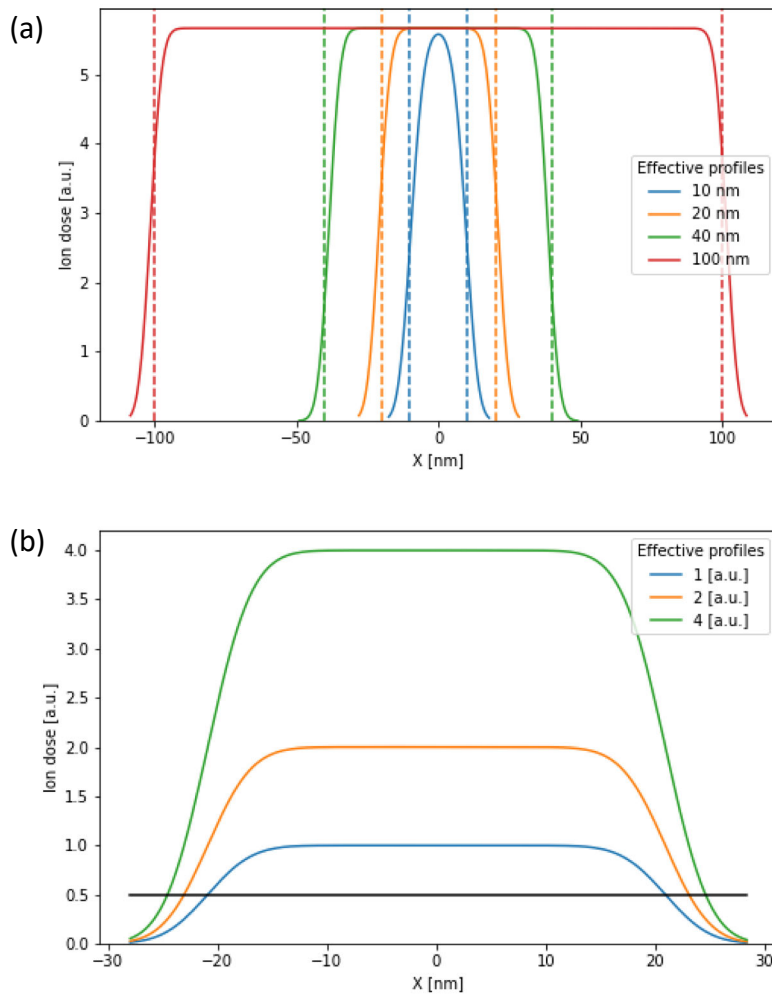
Figure S5: Radial line profiles computed from ion dose contour plots for (a) different disc diameters and (b) different total doses. The dashed vertical lines in (a) mark the nominal disc diameters and the black horizontal line in (b) marks an arbitrary threshold dose.

3. Additional data for experimental results of I-phase nucleation in supercooled VO_2

Figure S6 shows images at more temperatures in addition to what is shown in Figure 2b.
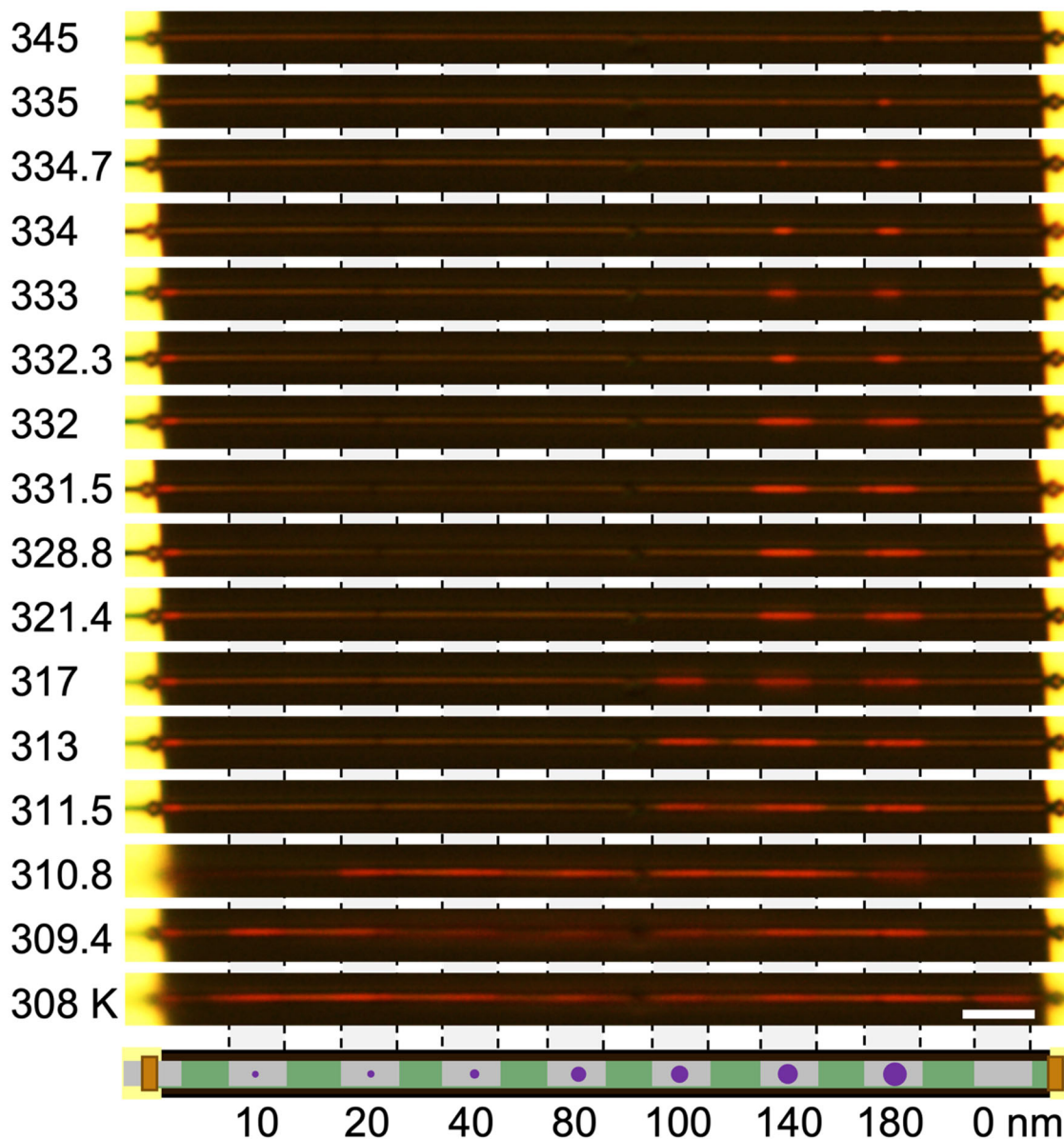
Figure S6: More data to Figure 2 demonstrating the I-phase nucleation process in a long, suspended VO2 nanobeam divided into eight pristine segments by He⁺ irradiation. The nucleation seeds have different diameter from 10 to 180 nm with the same Ga+ irradiation dose at 2×10¹⁶ ions/cm². Scale bar is 5 μm.

Figure S7 includes more doses for Figure 2d. Dose of 1.1, 2.2 and 4.4×10¹⁶ ions/cm² are systematically measured. Dose of 3.3, 5.5, 6.6 and 8.8×10¹⁶ ions/cm² are supporting data with only a few measurements.
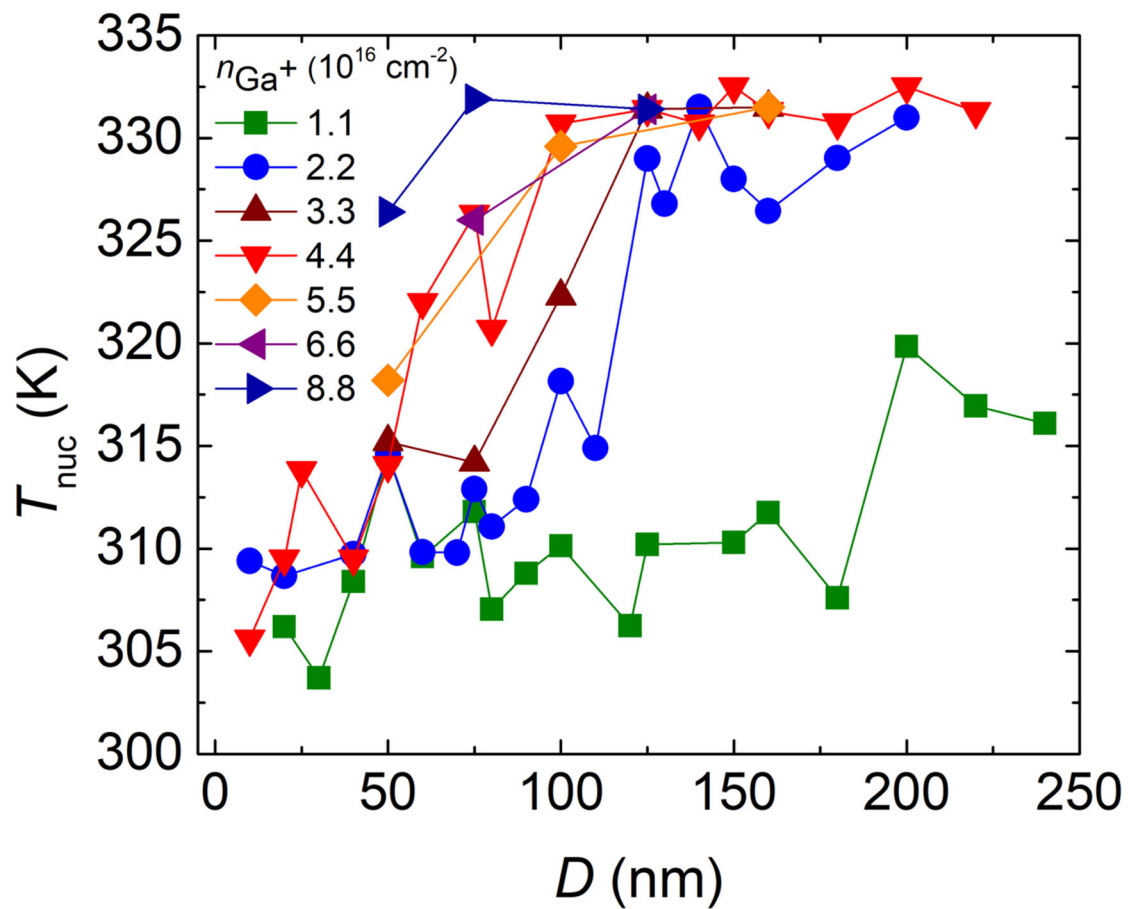
Figure S7: Complete data for Figure 2d with supporting data measured with nucleation seeds at doses of 3.3, 5.5, 6.6 and 8.8×10^16 ions/cm^2.

References

1. F. I. Allen, A review of defect engineering, ion implantation, and nanofabrication using the helium ion microscope. *Beilstein Journal of Nanotechnology* **12**, 633-664 (2021).

2. H. Mei *et al.,* Tuning Carrier Density and Phase Transitions in Oxide Semiconductors Using Focused Ion Beams. *Nanophotonics* **11**(17), 3923–32 (2022).

3. J. Rensberg *et al.*, Active Optical Metasurfaces Based on Defect-Engineered Phase-Transition Materials. *Nano Letters* **16**(2), 1050–55 (2016).

4. J. F. Ziegler, M. D. Ziegler, J. P. Biersack, SRIM–The stopping and range of ions in matter (2010). *Nuclear Instruments and Methods in Physics Research Section B: Beam Interactions with Materials and Atoms* **268**, 1818-1823 (2010).